41st Aerospace Sciences Meeting and Exhibit
6-9 January 2003, Reno, Nevada

AIAA 2003-790

Leading Edge Receptivity of Görtler Vortices in a Mach 15 Flow over a Blunt Wedge

Chong W. Whang * **and Xiaolin Zhong** †
University of California, Los Angeles, California 90095

Abstract

Longitudinal counter rotating streamwise vortices appear in boundary layer flow along a concave surface which are Görtler vortices, and they can play a key role in the instability and transition of boundary layers along a concave surface. In hypersonic boundary layers along the concave surface, multiple instability waves may co-exist e.g. first mode, higher harmonic boundary layer modes (second, third mode etc.) and Görtler mode. Forcing disturbances initially enter the boundary layers and generate instability waves which is called receptivity. In receptivity to free-stream disturbances, perturbations in free stream enter boundary layers and excite instability waves in boundary layers. It helps to study the naturally generated instability modes in boundary layers. In this paper, we present results of leading edge receptivity of Görtler vortices in a Mach 15 flow over a blunt wedge. Forcing disturbances are standing or traveling vorticity waves imposed in the free stream. Receptivity results of free stream standing vorticity waves show that the disturbances can be excited near the leading edge and in concave region. The growing disturbances near the leading edge are associated with the early transient growth due to the coupling of non-orthogonal eigenvectors. Growing disturbances in concave region is due to the Görtler instability. The vorticity waves with frequency do not excite the Görtler vortices along a concave surface inside boundary layers. The main conclusion of this receptivity study is that the Görtler vortices are mainly induced by free-stream standing vorticity waves. The traveling vorticity waves is difficult to penetrate into the boundary layers, while standing vorticity waves can excite growing disturbances inside boundary layers near the leading edge which excite the Görtler modes in concave region.

1 Introduction

In hypersonic boundary layers, there exist higher harmonic boundary layer modes (second, third mode etc.) as well as the first mode. If the flow is associated with the concave surfaces, Görtler mode also exists. It is important to study the roles of these instability modes in transition of boundary layers. Nayfeh [3], in his multiple-scale analysis for two dimensional boundary layers, showed that Görtler vortices can interact with the oblique Tollmien-Schlichting (TS) waves whose spanwise wavelength is the twice of the vortices. He found that Görtler vortices strongly destabilize the TS waves. Malik [4] obtained the results which are not agreed with Nayfeh. He found the inconsistent length scale in Nayfeh's formula and showed in his temporal and parallel analysis that the oblique TS waves whose wavelength is the half of the vortices are destabilized by the nonlinear interaction. Nayfeh and Al-Maaitah [5] corrected the formula and presented the new results which are the same to Malik [4]. They used both Floquet theory and the method of multiple-scale and showed both methods give a good agreement. Malik and Hussaini [6] considered nonlinear interaction between two dimensional TS waves and Görtler vortices. In the analysis, incompressible Navier-Stokes equations are solved using a Fourier-Chebyshev spectral method. It is shown that the TS waves can be excited by Görtler vortices, and due to the nonlinear effects, Görtler vortices induce the oblique wave whose wavelength is the equal to the vortices.

We had studied linear and non-linear Görtler instabilities and its interactions with other instability waves in hypersonic boundary layers by imposing the Görtler and other instability modes obtained from LST at the inlet of the computational domain [7–9]. By adding the modes obtained from LST at the inlet, we could observe developments of Görtler and other instability modes and their interactions at hypersonic speed. It was found that in a Mach 15 flow over a blunt wedge, unstable first and second Görtler modes exist in concave region [7]. The stable second mode was found and its interactions with Görtler mode has also been investigated [8]. The results showed that their interactions are weak although inflection profiles by nonlinear Görtler vortices have destabilizing effects on the second mode. In the previous studies, Görtler modes were the most dangerous instability waves in a Mach 15 flow over a blunt wedge. However, such studies could not explain the procedure of naturally developed Görtler vortices and other instability waves. In receptivity, external forcing disturbances enter boundary layers and excite instability waves. It helps to understand naturally developed flow instabilities in boundary layers. In receptivity to free stream disturbances, free stream forcing waves enter the boundary

*Graduate Student, e-mail: chong@seas.ucla.edu, Student Member AIAA
†Professor, Mechanical and Aerospace Engineering Department, Associate Fellow AIAA

layers and excite the most dominant instability waves inside boundary layers.

There are many difficulties in the experimental studies of high speed receptivity phenomena. For example, it is difficult to generate controllable disturbances with a well defined and independently variable frequency. Therefore, Direct Numerical Simulation becomes an useful tool in order to investigate supersonic and hypersonic receptivity process. Lin et al [10] solved compressible linearized Navier-Stokes equations and studied the receptivity of hypersonic boundary layer to different external disturbances. Zhong [11] studied the acoustic receptivity of hypersonic flow over blunt wedge by solving the full Navier-Stokes equations. It was shown that the interaction of free stream acoustic wave with bow shock generate instability waves behind the shock.

There have not been many studies in receptivity of Görtler instability. Hall [12] studied free-stream receptivity of Görtler vortices in incompressible boundary layers. He allowed the vortex to be generated by free-stream disturbances imposing at the leading edge and showed that Görtler vortices can be generated by receptivity of free-stream disturbances. Denier et al [13] addressed receptivity issue by considering the vortex motion induced by wall roughness and showed that wall roughness induces the Görtler vortices.

There are four kinds of weak perturbation waves in a uniform flow in the free stream: fast acoustic waves, slow acoustic waves, entropy waves, and vorticity waves. Acoustic waves enters boundary layers and excite T-S waves, therefore, in fast acoustic wave studies [14], pure Görtler mode could not be obtained. In addition, Görtler vorticies are standing waves which are independent of time. Standing forcing waves can be generated by free stream vorticity or entropy waves. In this paper, receptivity to free stream vorticity waves are investigated by solving the full Navier-Stokes equations using a high order shock fitting scheme.

2 FORMULATION

A. Direct Numerical Simulation

Receptivity to free stream disturbances is numerically simulated using a fifth order upwind shock fitting scheme. The governing equations and numerical schemes are briefly summarized here. Details of the numerical method and code validation can be found in [15].

In the numerical simulation, the three-dimensional Navier-Stokes equations are written in conservative-law form as follows:

$$\frac{\partial U^*}{\partial t^*} + \frac{\partial F^*{}_j}{\partial x_j^*} + \frac{\partial F^*{}_{vj}}{\partial x_j^*} = 0 \tag{1}$$

where

$$U^* = \{\rho^*,\ \rho^* u_1^*,\ \rho^* u_2^*,\ \rho^* u_3^*,\ e^*\} \tag{2}$$

$$e^* = \rho^* (C_v^* T^* + \frac{1}{2} u_k^* u_k^*) \tag{3}$$

The flux vectors are

$$F^*{}_j = \begin{Bmatrix} \rho^* u_j^* \\ \rho^* u_1^* u_j^* + p^* \delta_{1j} \\ \rho^* u_2^* u_j^* + p^* \delta_{2j} \\ \rho^* u_3^* u_j^* + p^* \delta_{3j} \\ (e^* + p^*)\, u_j^* \end{Bmatrix} \tag{4}$$

$$F^*{}_{vj} = \begin{Bmatrix} 0 \\ \tau_{1j}^* \\ \tau_{2j}^* \\ \tau_{3j}^* \\ \tau_{jk}^* u_k^* - q_j^* \end{Bmatrix} \tag{5}$$

where

$$\tau_{ij}^* = -\mu^* \left(\frac{\partial u_i^*}{\partial x_j^*} + \frac{\partial u_j^*}{\partial x_i^*} \right) + 2\mu^* / 3 \frac{\partial u_k^*}{\partial x_k^*} \delta_{ij} \tag{6}$$

$$q_j^* = -\kappa^* \frac{\partial T^*}{\partial x_j^*} \tag{7}$$

μ^* is the viscousity coefficient and calculated using the Sutherland's law, and κ^* is the heat conductivity coefficient computed by assuming a constant Prandtl number Pr. The gas is assumed to be thermally and calorically perfect gas.

The general curvilinear three-dimensional coordinates (ξ, η, ζ, τ) are used along the body fitted grid lines. The shock fitting method treats the bow shock as a computational boundary at $\eta = \eta_{max}$. The flow variables behind the shock are determined by the Rankine-Hugoniot relation across the shock and a characteristic compatibility equation from behind the shock. The transformation relations for the current grid systems are

$$\begin{cases} \xi = \xi(x, y, z) \\ \eta = \eta(x, y, z, t) \\ \zeta = \zeta(x, y, z) \\ \tau = t \end{cases} \iff \begin{cases} x = x(\xi, \eta, \zeta, \tau) \\ y = y(\xi, \eta, \zeta, \tau) \\ y = y(\xi, \eta, \zeta, \tau) \\ t = \tau \end{cases} \tag{8}$$

where $\xi_t = 0$ and $\zeta_t = 0$ because the ξ and ζ grid lines are fixed when the shock boundary moves. In the numerical simulations, the governing equations (1) are transformed into the computational domain (ξ, η, ζ, τ).

$$\frac{1}{J}\frac{\partial U}{\partial \tau} + \frac{\partial E'}{\partial \xi} + \frac{\partial F'}{\partial \eta} + \frac{\partial G'}{\partial \zeta} + \frac{\partial E'_v}{\partial \xi} + \frac{\partial F'_v}{\partial \eta} + \frac{\partial G'_v}{\partial \zeta} + U \frac{\partial (\frac{1}{J})}{\partial \tau} = 0 \tag{9}$$

The governing equation (9) is discretized in the computational domain (ξ, η, ζ, τ). High order finite difference methods are used for spatial discretization of the equation. Inviscid and viscous flux terms are discretized using different methods: fifth order upwind explicit schemes for the inviscid flux terms and sixth order central difference schemes for the viscous terms. The

time advancement of the governing equations is solved by Runge-Kutta schemes.

B. Free stream forcing disturbances

Forcing disturbances are imposed by receptivity to free-stream disturbance waves. The wave fields are represented by perturbations of instantaneous flow variables with respect to the local steady base flow variables at the same location. There are four kinds of weak perturbation waves in a uniform flow in the free stream: fast acoustic waves, slow acoustic waves, entropy waves, and vorticity waves. The perturbation of an arbitrary flow variables can be written in the following form:

$$q'_\infty = |q_\infty| e^{i(\mathbf{k}_\infty \cdot \mathbf{x} - \omega t)} \tag{10}$$

where q'_∞ represents the perturbation of any flow variable, $|q_\infty|$ is the wave amplitude, $\mathbf{k}_\infty$ is the wavenumber, and ω is the wave frequency in the free stream before reaching the shock. Perturbation amplitudes of non-dimensional flow variables satisfy the following dispersion relations:
streamwise vorticity waves ($\omega = \mathbf{U}_\infty \cdot \mathbf{k}_\infty$):

$$\begin{aligned} |v'|_\infty k/k_y &= |w'|_\infty k/k_z = \epsilon c_\infty \ , \\ |u'|_\infty &= |p'|_\infty = |s'|_\infty = 0 \ ; \end{aligned}$$

entropy waves ($\omega = \mathbf{U}_\infty \cdot \mathbf{k}_\infty$):

$$\begin{aligned} |\rho'|_\infty &= |s'|_\infty = \epsilon c_\infty \ , \\ |u'|_\infty &= |v'|_\infty = |w'|_\infty = |p'|_\infty = 0 \ ; \end{aligned}$$

fast acoustic waves ($\omega = \mathbf{U}_\infty \cdot \mathbf{k}_\infty + c_\infty k$):

$$\begin{aligned} |\rho'|_\infty &= |p'|_\infty/\gamma = |u'|_\infty k/k_x = |w'|_\infty k/k_z = \epsilon c_\infty \ , \\ |s'|_\infty &= |v'|_\infty = 0 \ ; \end{aligned}$$

slow acoustic waves ($\omega = \mathbf{U}_\infty \cdot \mathbf{k}_\infty - c_\infty k$):

$$\begin{aligned} |\rho'|_\infty &= |p'|_\infty/\gamma = |u'|_\infty k/k_x = |w'|_\infty k/k_z = \epsilon c_\infty \ , \\ |s'|_\infty &= |v'|_\infty = 0 \ ; \end{aligned}$$

where ϵ is a number which controls a disturbance amplitude, and ϵc_∞ represents the relative amplitude of a free-stream wave. The parameter $\mathbf{k}_\infty$ is the free-stream wavenumber vector.

Acoustic waves enter boundary layers and mainly excite T-S waves; therefore, Görtler vortices are hardly generated by acoustic waves.[14] Görtler vortices are standing waves, and such vortices can be generated by the forcing waves with zero frequency. Free-stream acoustic waves cannot impose standing disturbances in boundary layers; therefore, acoustic waves cannot excite the pure Görtler mode in hypersonic boundary layers. Görtler vortices can be excited by free-stream vorticity waves, and we imposed streamwise free-stream vorticity waves to the 2-D base flow solution. In this paper, receptivity to standing and traveling free stream vorticity waves are investigated.

3 Results

The specific test case is a Mach 15 flow over a blunt wedge with a concave surface. The flow conditions in free stream are

$$\begin{aligned} &T^*_\infty = 101.059K \\ &P^*_\infty = 10.3Pa \\ &T^*_w = 1000K \\ &Re_\infty = \rho^*_\infty U^*_\infty/\mu^*_\infty = 150753.175/m \end{aligned} \tag{11}$$

The body surface is assumed to be a non-slip wall with an isothermal wall temperature T^*_w. Two-dimensional steady base flow along the blunt body with concave surface is first obtained by two-dimensional simulation. Three-dimensional simulation is carried out for receptivity to free stream. Figure 1 shows a schematic of computational domain of two-dimensional base flow and free stream receptivity of Görtler instability simulation.

3.1 Two-Dimensional Base Flow

LST analysis on the previous 2-D base flow [7–9] showed that the only Görtler mode is unstable, and other modes such as Mack's modes are stable in our computational domain, and the new sets of 2-D steady base flow with ten times higher Reynolds number is computed to check if the other instability modes can be found in high Reynolds number flows. In the simulation, we have enlarged the body size ten times with the same flow conditions in free stream. Seven computational zones are used in the new two-dimensional steady flow calculations which are resolved by a total of 2253 $\times$ 241 grids. First three zones are parabolic blunt body given by $x = by^2 - d$ where b and d are the given constants 4.0 and 1.0 respectively. The concave surface is extended in the following zones. The concave body surface is defined by two piecewise-polynomial equations: $y = a_1x^3 + a_2x^2 + a_3x + a_4$ and $y = b_1x^2 + b_2x + b_3$ where the coefficients are determined to maintain the continuous conditions for the zeroth, first, and second order derivatives of the surface functions in order to get continuous radius curvature which is a function of the first and second order derivatives. Resulting local Reynolds number is up to 6×10^6. Local Reynolds number is calculated using the flow properties behind the bow shock as $Re_x = \rho^* U^* x^*/\mu^*$, where ρ^*, U^*, and μ^* are density, velocity, and viscosity respectively, and x^* is the horizontal distance from the blunt nose. Reynolds number of the resulting 2-D base flow is ten times larger than the previous [7–9]. Magnitude of Görtler number is the almost same becasue radius of curvature is five times larger than previous.

Figure 2 shows the numerical solutions of the new two-dimensional steady flow. Pressure is nondimensionalized using free stream flow variable: P^*_∞. Reference length is the horizontal distance from the blunt nose to the starting point of the concave surface. Basic structure of the pressure is similar to the previous

low Reynolds number case [7], but Reynolds number is ten times larger. The figure shows the adverse pressure gradient in concave region.

Having obtained the new 2-D base flow, spatial linear stability analysis for the computed two-dimensional steady base flow is applied at $X = 3.0$ to find instability waves. In the LST analysis, spanwise wave number β is given, and complex α and corresponding eigenfunctions are computed for various frequencies. The detailed method and its validation of LST analysis can be found in Ref. [7]. At zero wave frequency (ω), we found unstable Görtler modes in concave region. We have also investigated other instability modes at various frequencies in concave region. Figure 3 shows the growth rates (α_i) for various wave modes with respect to wave frequencies. Growth rates and frequencies are nondimensionalized by streamwise velocity behind the shock and streamwise distance. At this location, there is unstable frequency range for $ModeI$ ($30 < \omega < 70$), but other modes are still stable. Unstable Görtler mode is also shown in the figure. It shows that Görtler mode is still the most dangerous mode in concave region for a high Reynolds number flow.

3.2 Receptivity to Standing Vorticity Waves

Receptivity to free-stream vorticity waves with zero wave frequency is first investigated since streamwise vorticity with zero frequency is a characteristic of Görtler vortices. Spanwise wavenumber, wave angle and nonlinear effects of the standing vorticity waves are studied by solving the full Navier-Stokes equations.

First, spanwise wavenumber effects of the free-stream receptivity on Görtler vortices are investigated. We have simulated four cases with different spanwise wavenumber of standing vorticity waves ($\beta = 0.05, 0.1, 0.15, 0, 2$). Spanwise wave number, β, is normalized by the characteristic boundary layers thickness at $X = 3.0$. Wave angle, θ, with respect to the spanwise direction is 30°. Normal and spanwise components of a wavenumber vector are as follows:

$$k_y = k\sin(\theta) \quad , k_z = k\cos(\theta) \quad . \tag{12}$$

In the free stream, nonzero disturbance variables are normal and spanwise velocity disturbances (v' and w'), and nonzero wavenumbers are normal and spanwise components (k_y and k_z). Amplitudes of other disturbance variables and streamwise wavenumber are zero. Zero streamwise wavenumber gives zero wave frequency. Resulting free-stream forcing waves are streamwise vorticities with zero frequency which can generate Görtler vortices along the concave surface inside hypersonic boundary layers. Amplitudes of free-stream disturbances are $10^{-4}c_\infty$ where c_∞ is a speed of sound in free stream. Weak disturbance amplitudes ensure that the generated instability waves are linear, and four Fourier collocation points in spanwise direction are used to compute one spanwise wave length of the disturbances.

Figure 4 shows streamwise velocity perturbation contours of the first computational zone at $\beta = 0.1$. The flow is simulated until it reaches a steady state condition since the imposed vorticity waves are steady. Free-stream standing vorticity waves pass the bow shock, penetrate into boundary layers, and excite the unstable wave modes inside the layers. According to LST analysis, this early region is stable, but the simulation results show that the standing vorticity waves generate the instability waves near the leading edge inside boundary layers. Other simulations with different spanwise wave number show the same mechanism of growing disturbances near the leading edge. The growing disturbances near the leading edge may be associated with the early transient growth which is due to the coupling of non-orthogonal eigenvectors. Hanifi et al [1] and Reshotko [2] showed such transient growth in compressible boundary layer flow. They found that the optimal disturbances are stationary with zero frequency and a particular spanwise wave number. The imposed vorticity waves in our simulations have zero frequency and non-zero spanwise wave number which are the optimal disturbances. Theoretical studies on the early transient growth [1,2] showed that the growth mechanism results from fluid particles moved away from or toward the wall which is so called lift-up effect. Lift-up effect can also be found in Görtler instability. In Ref. [8], we have showed that Görtler vortices pump vertically the low-speed fluid away from the wall and push the high speed fluid toward the wall which is the lift-up effect.

We have simulated the receptivity to standing vorticity waves until those propagate at the end of the computational domain and reach steady state conditions for seven computational zones for four wavenumber cases of the standing vorticity waves. Figure 5 shows surface shape of the blunt body and streamwise distributions of streamwise velocity and temperature perturbations inside boundary layers for the standing vorticity waves with $\beta = 0.1$. Four curves represent four Fourier collocation points. The figure shows that the disturbances increase near the leading edge but decay before they reach the concave surface region. Figure 5 also shows growing disturbances in concave region. Concave surface starts at $X = 1.0$ as shown in Fig. 5, and after the body shape becomes concave, the amplitudes of disturbances are amplified as the flow moves downstream. Growing disturbances in concave region are associated with the Görtler instability. The distribution curves indicate that disturbances keep growing as long as the body surface is concave. Görtler number increases downstream due to the increase of local Reynolds number; therefore, Görtler mode becomes more unstable as X increases.

Fourier analysis in spanwise direction is carried out on the numerical solutions of the standing vorticity waves. Fourier transform of a disturbance variable is expressed

to:

$$q'(x,y,z) = \sum_{n=0}^{N} |q'_n| \, e^{i\,[n\beta z + \phi_n]} \qquad (13)$$

where β is the spanwise wavenumber of disturbance, and $q'(x,y,t)$ represents any perturbation variables. $|q'_n(x,y)|$ and $\phi_n(x,y)$ are the local perturbation amplitudes and phase angles respectively. The integer n represents the wave modes of the perturbation fields. $n = 1$ represents a fundamental mode. Figure 6 shows amplitude contours of velocity disturbances ($|A| = \sqrt{|u'_n|^2 + |v'_n|^2 + |w'_n|^2}$) at $\beta = 0.1$ obtained by Fourier analysis for the total computational zones. Amplitudes are normalized by free-stream forcing disturbance amplitudes. The figure shows the development of vorticity layer inside boundary layers induced by free stream standing vorticity waves. It also shows that disturbance amplitude keep increasing in concave region since the maximum amplitude occurs at the end of the computational domain. Growing disturbance amplitude in concave region is due to the Görtler instability.

In LST analysis on the 2-D base flow, we found unstable Görlter modes with a specific spanwise wave number. The LST results are compared with those from Fourier analysis of DNS results. Figure 7 shows growth rate distributions obtained from LST with respect to X for the four different spanwise wave numbers. It shows that at $\beta = 0.1$, the Görtler mode has the maximum growth rate which implies that the Görtler mode at $\beta = 0.1$ is the most unstable in our flow conditions. The figure also shows that Görtler modes become more unstable as the flow moves downstream since Görtler number increases. Eigenfunctions of DNS results obtained from Fourier analysis are compared with those from LST to verify if the generated instability waves by the free-stream standing vorticity waves are Görtler vortices. Figure 8 shows the comparisons of eigenfunctions from LST with those induced by the standing vorticity waves with $\beta = 0.1$ located at $X = 3.0$. Streamwise and normal velocity and temperature disturbances are compared in the figure. Eigenfunctions are normalized by pressure perturbation at the surface. It shows that the structures inside boundary layers are comparable which represents that the stationary free-stream vorticity waves can excite Görtler mode inside boundary layers in concave region. From this result, we conclude that the growing mechanism in concave region shown in Fig. 5 is associated with the Görtler instability.

Fourier analysis is conducted for all four different spanwise wavenumber cases. Figure 9 shows streamwise velocity disturbance amplitude contours in convex region including a blunt nose at four different spanwise wavenumbers. The amplitudes are normalized by the one for free-stream forcing disturbance. All four contours show that disturbances are amplified near the leading edge. Growing disturbances are well represented by intensity for all four cases which implies that the instability waves are generated by the standing vorticity waves. However, the locations of the maximum amplitude are different depending on the value of spanwise wavenumber. As β increases, its location moves closer to the leading edge. At $\beta = 0.05$, the maximum location occurs at $X \approx 1.0$ while at $\beta = 0.2$, it appears much closer to the leading edge located at $X \approx 0.4$. The figure also shows that after the amplitude reaches the maximum, it starts decaying. If the maximum location occurs earlier, disturbances decay faster. It is well represented in the figure. At the end of the contours, disturbances at $\beta = 0.2$ contain the weakest energy since its maximum location occurs the earliest among the four cases. Figure 10 shows contours of the disturbance amplitudes in concave region at four different spanwise wave numbers. All four cases show the growing disturbances in concave region. The maximum disturbance occurs at the end of computational domain which represents that disturbances keep increasing as the flow moves along the concave surface. The growing mechanism in concave region is due to the Görtler instability, and since Görtler number increases as the flow moves downstream, disturbances keep increasing.

Figure 11 shows the streamwise distributions of the maximum velocity disturbance amplitude ($|A| = \sqrt{|u'_n|^2 + |v'_n|^2 + |w'_n|^2}$) inside the boundary layers obtained by Fourier analysis of DNS results. It clearly shows that standing vorticity waves excite instability waves near the leading edge which decay after they reach the maximum amplitudes, and before they reach the concave surface region. The growing disturbances near the leading edge are due to the early transient growth, and those in concave region ($X > 1.0$) is due to the Görtler instability. Figure 11 shows that the vorticity wave at $\beta = 0.2$ induces the largest amplitude disturbances by the early transition but the weakest growing process in concave region. It also shows that the smallest amplitude disturbances by the transition at $\beta = 0.05$ can excite the most amplifying Görtler mode since the largest disturbance amplitude reach at the end of the computational domain. It may be explained by the linear stability analysis and relationship between early transition and concave surface. Figure 7 shows that the Görtler mode at $\beta = 0.1$ has the largest growth rate, while the one at $\beta = 0.2$ has the smallest. A growth rate can be calculated by the slope of disturbance amplitude curve. Figure 11 shows that the most stiff curve occurs at $\beta = 0.1$ while the least is at $\beta = 0.2$ which is consistent with the LST results. However, at $\beta = 0.05$, amplitude of the Görtler mode excited by the vorticity waves is larger than the one at the $\beta = 0.1$. The reason is currently not clear, but it may be explained by the relationship between the early transient growth and a concave surface. Figure 11 shows that as spanwise wavenumber increases, the maximum amplitude of disturbances by the early transition increases,

and its location is more closer to the leading edge as we discussed in Fig. 9. At $X = 1.0$, disturbance amplitude at $\beta = 0.2$ is the smallest which represents that decaying procedure starts at earlier location as β increases. At $\beta = 0.05$, the maximum amplitude induced by the early transition is the smallest, but its location is closer to the concave surface located at $X = 1.0$. Before the decaying procedure of the early transient is initiated, the concave surface develops; therefore, at $\beta = 0.05$, more disturbance energy can be excited by Görtler instability, and the largest amplitude's waves are generated.

Figure 11 shows that the slope at $\beta = 0.05$ is, however, smaller than the one at $\beta = 0.1$ as predicted by LST analysis. In the linear region, Görtler mode at $\beta = 0.1$ will overtake the one with $\beta = 0.05$ as the flow moves downstream. The early transient studies [1,2] showed that the optimal disturbance can excite $2 - 3$ order larger disturbance inside boundary layers. If the amplitude reaches the limit in which the waves have the enough energy to become nonlinear, the case at $\beta = 0.05$ could break down to turbulence earlier than the one at $\beta = 0.1$.

The growing mechanism of the early transient growth is due to the lift-up effect, and such effect is also observed in the Görtler instability. We have studied relationships between two different growing mechanisms and found that those are closely related. Figure 12 and 13 show streamwise velocity and temperature perturbation contours in two different regions which are convex and concave region. Disturbances in convex region are due to the early transition, and those in the concave are due to the Görtler instability. Inside boundary layers, basic structures of the perturbations in convex and concave region are the same. It implies that instability waves induced by the early transition and the Görtler instability may be the same. Figure 14 shows the streamwise vorticity contours at four different streamwise locations. Dashed lines in the figure represent negative values. The figure indicates that the instability waves inside boundary layers are counter rotating vortices in both convex and concave regions since the streamwise vorticity is anti-symmetric in spanwise direction. Streamwise vorticity contours also show that both growing mechanisms are closely related since their structures inside boundary layers are comparable. Figure 15 and 16 are the wall normal distributions of streamwise velocity and temperature perturbation amplitudes obtained from Fourier analysis. The mode structures inside boundary layers are the same in convex and concave regions. From our numerical results, we conclude that the growing mechanism due to the early transient growth is consistent with the one in the Görtler instability.

Effects of wave angle, θ, are also investigated. At $\theta = 0°$, nonzero wave number and free-stream disturbance variable are k_z and normal velocity, and those at $\theta = 90°$ are k_y and spanwise velocity. In the simulations, four different wave angles are considered ($\theta = 0°, 30°, 60°, 85°$). According to LST analysis, Görtler mode is the most unstable at $k_z = 0.1$, and k_z is fixed to 0.1 for all cases. As the angle increases, normal component wave number, k_y, increases. The amplitudes of free-stream disturbances are fixed as $10^{-4}c_\infty$ so that developments of waves are linear. Figure 17 shows contours of streamwise velocity disturbance amplitude in convex region including a blunt nose at four different forcing wave angles. The contours show that as the angle increases, the early transition is initiated at later location. At $\theta = 0°$, the first peak occurs at $x \approx 0.25$ while at $\theta = 60°$, it is at $x \approx 1.0$. The figure shows that disturbances decay after they reach the peak. However, at $\theta = 85°$, before the amplitude reaches the first peak, a body surface become concave, therefore, the contours do not show the the region of decaying disturbances which represents that the maximum location occurs at much later location. Figure 18 shows contours of streamwise velocity disturbance amplitude in concave region at four different forcing wave angles. As the spanwise wave number studies, all four cases show the similar results. Although the strength of the disturbances in boundary layers are different depending on the value of wave angle, the generated waves are amplified as long as the surface is concave for all four different wave angle studies due to the Götler instability. A radius of curvature does not change much, but local Reynolds number increases as the flow moves downstream. As a result, Görtler number increases with respect to X, and Görtler modes become more unstable as X increases. It is true in all different wave angle studies.

Figure 19 shows the streamwise distributions of the maximum velocity disturbance amplitude ($|A| = \sqrt{|u_n'|^2 + |v_n'|^2 + |w_n'|^2}$) for the different wave angles. All the cases show the growing mechanisms induced by the early transition and the Görtler instability. The figure shows that at $\theta = 0°$, a growing procedure due to the early transition is initiated faster than the other cases since the amplitude reaches the peak at the earliest streamwise location. As the angle increases, it becomes slower since its location moves more downstream. At $\theta = 30°$, a disturbance amplitude grows slower than the one at $\theta = 0°$ but faster than the one at $\theta = 60°$ at the beginning of the growing procedure. However, after a short distance from the leading edge, disturbances at $\theta = 60°$ overtake those at $\theta = 30°$, and as the flow moves further, the disturbances grow more than those at $\theta = 0°$. It implies that there is an optimal wave angle in which disturbances are the most unstable in the early transient growth. In our flow condition with $k_z = 0.1$, $\theta = 60°$ is the most dangerous wave angle. The weakest growing procedure occurs at $\theta = 85°$ in wave angle studies. The amplitude curves shows that the early transient growth at $\theta = 85°$ is initiated after

some distance away from the leading edge. It may be due to two-dimensional wave direction. According to theory, the optimal disturbances of the early transient growth are stationary with a particular spanwise wave number which represents spanwise direction propagations of disturbances are significant. At $\theta = 90°$, spanwise wavenumber cannot be imposed since $k = k_y$. At $\theta = 85°$, the direction of the free-stream forcing waves is almost two-dimensional since k_y is much bigger than k_z. However, the forcing waves still have a component of spanwise wave number, and the early transient growth is observed at this angle.

Figure 19 also shows that disturbances grow in concave region ($X > 1.0$) due to the Görtler instability. At the all wave angles, disturbances are excited as the flow moves downstream by concave effects. The figure shows that at $\theta = 60°$, the disturbances are the most amplified, and as the angle decreases, growing procedure becomes weaker. The reason is not clear, but it may be due to the location of the concave surface. At $\theta = 60°$, the first peak point of the disturbance amplitude occurs at $X = 0.7$, but the one at $\theta = 0°$ does at $X = 0.2$. It represents that the decaying procedure at $\theta = 60°$ occurs at later location which is closer to the concave surface. Therefore, more energy of the disturbances can be excited by concave surface. As a result, the most unstable Görtler mode is excited by free-stream standing streamwise vorticity waves at $\theta = 60°$ in our flow conditions. The disturbances at $\theta = 85°$ shows the weakest growing by early transition, and those contain the least disturbance energy at the location of concave surface; therefore, the generated Görlter mode at $\theta = 85°$ is the weakest.

For weak free-stream forcing waves, generated instability waves inside boundary layers are expected to be linear. In previous simulations of receptivity to the standing vorticity waves, ϵ is 10^{-4} in which we assumed that the forcing waves are weak. Figure 20 shows distributions of maximum disturbance amplitude for fundamental mode ($n = 1$) and mean flow correction mode ($n = 0$) obtained by Fourier analysis of DNS results at $\beta = 0.1$ and $\theta = 30°$. The fundamental amplitude is four order higher than the mean mode which represents that at $\epsilon = 10^{-4}$, all higher harmonic modes are negligible, and the generated instability modes are linear.

As ϵ increases, the receptivity results deviate from the linear curves due to the interaction between the wave harmonics, and the nonlinear effects become significant. For the nonlinear receptivity studies, standing vorticity waves with two different forcing wave amplitudes ($\epsilon = 10^{-1}, 5 \times 10^{-3}$) are simulated. Eight Fourier collocation points in spanwise direction are used in nonlinear receptivity simulations in order to resolve two more higher harmonic modes as well as the fundamental and mean modes. Figure 21 shows distributions of disturbance amplitudes obtained by Fourier analysis at two different ϵ. Mean flow correction ($n = 0$) and second harmonic ($n = 2$) modes show the same order of disturbance amplitude for both ϵ. Third harmonic contains lower disturbance energy than the second as expected. As ϵ increases, amplitudes of higher harmonic modes and the mean mode become closer to the fundamental mode, and the third mode is closer to the second which represents that nonlinear effects become more significant. Amplitudes of the fundamental modes ($n = 1$) do not change much, but when we closely examine the curves, as ϵ increases, the energy of the fundamental mode decreases which implies that the fundamental energy is transferred to the higher harmonic and the mean modes. Although the numerical results show that the higher harmonics increase as ϵ increase, the fundamental mode is the most important mode for both ϵ. At $\epsilon = 0.1$, the fundamental mode contains one order higher energy than the second harmonic mode. As a result, the strong nonlinear effects discussed in Ref. [8] are not observed. However, the results show that as the forcing amplitude increases, nonlinear effects become more significant. Figure 22 shows contours for the streamwise mean velocity, which is the sum of two-dimensional base flow and the generated disturbances, at the end of computational domain. At $\epsilon = 0.1$, two-dimensional base flow is distorted while at $\epsilon = 5 \times 10^{-3}$, the mean structure is two-dimensional which indicates that as a forcing amplitude increases, the base flow can be distorted as shown in Ref. [8].

3.3 Receptivity to Traveling Vorticity Waves

Having studied receptivity of free-stream standing vorticity waves, traveling vorticity waves with nonzero frequencies are investigated. Streamwise wavenumber, k_x, is not zero which induces nonzero wave frequency in the free stream. Three different wave frequencies ($\omega = 10, 25, 50$) are concerned in our simulations. Frequencies are nondimensionalized by streamwise velocity behind the shock and streamwise distance at $X = 3.0$. Spanwise wavenumber and wave angle are 0.1 and 30° respectively. In all cases, amplitudes of free-stream disturbance are $10^{-4} c_\infty$ where c_∞ is a speed of sound in free stream. The simulation results show that the effects of the early transient growth for the traveling streamwise vorticity waves are weaker than those for the standing waves. The results also show that Görtler mode is hardly excited by the traveling waves.

Fourier analysis is carried out on the numerical results of receptivity to traveling vorticity waves. Fourier transform of a disturbance variable is expressed to:

$$q'(x, y, z, t) = \sum_{m=0}^{M} \sum_{n=0}^{N} q'_{mn}(x, y) e^{i\,[m\omega t + n\beta z + \phi_{mn}]} \quad (14)$$

where β and ω is the spanwise wave number and frequency of the disturbances, and $q'(x, y, z, t)$ represents any perturbation variables. $q'_{mn}(x, y)$ and ϕ_{mn} are the local perturbation amplitudes and phase angles. The

integer m and n represent the wave mode of the perturbation fields. In our numerical results, the fundamental wave mode is $(m, n) = (1, 1)$.

Figure 23 is streamwise distributions of the maximum disturbance amplitudes of the fundamental mode ($m = 1$ and $n = 1$ in Eq.(14)) inside boundary layers for three different free-stream wave frequencies. Those for the standing vorticity waves with the same spanwise wavenumber and wave angle are also plotted in the figure for the comparison. All three traveling vorticity waves also show the growing disturbances near the leading edge due to the early transient growth, but their effects are much weaker than those for the standing waves. The figure shows that as the frequency decreases, such effects become stronger. According to the theoretical studies of the early transient growth [1, 2], the optimal disturbances are stationary with zero frequency which is coincident with our numerical results.

Figure 24 shows instantaneous cross sectional contours of streamwise velocity perturbations for the traveling and standing vorticity waves of the first computational zone. Contours for the traveling vorticity waves at $\omega = 10$ and $\omega = 25$ after the numerical results reach a periodic condition and those for the standing waves are shown in the figure. At $\omega = 25$, most disturbances behind the shock are outside the boundary layers. At $\omega = 10$, some disturbances penetrate into boundary layers, but main structure of the disturbances are outside boundary layers. However, for the standing vorticity waves ($\omega = 0$), most disturbances penetrate into the layers and excite the growing vorticity layers. From these results, we conclude that the traveling vorticity waves are hard to penetrate into boundary layers; therefore, the effects of the early transient growth are weak compared with the standing waves.

We have investigated that free-stream receptivity to traveling vorticity waves also excite disturbances inside boundary layers by the early transient growth; however, Fig. 23 shows that there is no growing mechanism of Görtler instability. It shows that disturbance amplitudes are not affected by a concave surface in the traveling vorticity wave studies.

Figure 25 shows comparison of the maximum disturbance amplitudes of the zeroth mode ($m = 0$ and $n = 1$) for the traveling vorticity waves with those for the standing waves. $m = 0$ and $n = 1$ represents the fundamental mode for the standing vorticity waves which are the Görtler modes. Amplitude of the zeroth mode of the traveling waves is four order smaller than the one of the standing waves. The free-stream forcing disturbances are weak so that the disturbances are in the linear region; therefore the zeroth mode for traveling waves is the numerical noise. The figure shows that such random noise grows in concave region which implies that standing disturbances can be excited by a concave surface. From this result, we conclude that the concave surface effects are strong on the standing waves. The traveling vorticity wave studies show that Görtler modes are hardly excited by the traveling waves since Görtler vortices are standing waves.

4 Summary and Future Works

Leading edge receptivity of Görtler vortices in hypersonic boundary layers has been studied using numerical simulations. Free-stream forcing waves were standing and traveling streamwise vorticity waves. The free-stream vorticity waves were imposed at leading edge and throughout all computational domain. The waves interacted with a bow shock, entered the boundary layers and excited the instability waves inside boundary layers. The receptivity results of the standing vorticity waves showed that the forcing waves excite the instability waves inside boundary layers near the leading edge and in concave region. It was found that growing disturbances near the leading edge are associated with the early transient growth due to the coupling of non-orthogonal eigenvectors. Theoretical studies [1,2] showed the optimal disturbances of the transient growth are stationary with zero frequency and a particular spanwise wave number which can be generated by the free-stream standing streamwise vorticity waves. Instability waves were also found in concave region due to the Görtler instability. The eigenfunctions of perturbations obtained by Fourier analysis of the DNS results were compared with those obtained by LST. They agreed well inside boundary layers which implies that the generated instability waves in concave region are Görtler vortices. The relationships of these two growing mechanisms were investigated by comparing the numerical results near the leading edge and in concave region. All the results were coincident which represent both mechanisms are closely related.

Receptivity results of the traveling vorticity waves showed that wave frequency reduces effects of the early transient growth since as the frequency increased, maximum disturbance amplitude due to the early transient growth decreased. The results also showed that Görtler voritices could not be generated by the traveling vorticity waves. The main conclusion of this receptivity study is that the Görtler vortices are mainly induced by free-stream standing vortices. The traveling free-stream vortices induce very weak Görtler vortices in the boundary layer. The traveling vorticity waves is difficult to penetrate into the boundary layers since most disturbances are outside the boundary layers, while standing vorticity waves can excite growing disturbances inside boundary layers near the leading edge which excite the Görtler modes in concave region. We also conclude that the early transient growth is closely related to the Görtler instability.

Results of receptivity to traveling vorticity waves showed that the mean flow correction modes are excited by Görtler instability. Nonlinear effects of traveling vor-

ticity waves will be studied in which the mean mode becomes significant. Steady forcing free-stream disturbances can also be generated by entropy waves. The effects of entropy waves on the early transient growth and Görtler instability will be investigated by solving the full Navier-Stokes equations.

Acknowledgments

This work was sponsored by the Air Force Office of Scientific Research, USAF, under AFOSR Grant # F49620-00-1-0101 monitored by Dr. John Schmisseur. The views and conclusions contained herein are those of the author and should not be interpreted as necessarily representing the official policies or endorsements either expressed or implied, of the Air Force Office of Scientific Research or the U.S. Government. The numerical simulations were performed on the IBM SPs at cfdlab in UCLA and at the NAVO MSRC.

References

[1] Hanifi, A., Schmid, P., and Henningson, D., "Transient growth in compressible boundary layer flow," *Phys. Fluids*, Vol. 8(3), 1996, pp. 826–837.

[2] Reshotko, E., "Transient growth: A factor in bypass transition," *Phys. Fluids*, Vol. 13(5), 2001, pp. 1067–1075.

[3] Nayfeh, A. H., "Effect of streamwise vortices on Tollmien-Schlichting waves," *J. Fluid Mech.*, Vol. 107, 1981, pp. 441–453.

[4] Malik, M. R., "Wave interaction in three dimensional boundary layers," *AIAA Paper 86-1129.*, 1986.

[5] Nayfeh, A. H. and Al-Maaitah, A., "Influence of streamwise vortices on Tollmien-Schlichting waves," *Phys. Fluids*, Vol. 31(12), 1988, pp. 3543–3549.

[6] Malik, M. R. and Hussaini, M. Y., "Numerical simulation of interaction between Görtler vortices and Tollmien-Schlichting waves," *J. Fluid Mech.*, Vol. 210, 1990, pp. 183–199.

[7] Whang, C. and Zhong, X., "Direct Numerical Simulation of Görtler Instability in Hypersonic Boundary Layers," *AIAA 99-0291*, 1999.

[8] Whang, C. and Zhong, X., "Nonlinear Interaction of Gortler and Second Shear Modes in Hypersonic Boundary Layers," *AIAA 2000-0536*, 2000.

[9] Whang, C. and Zhong, X., "Secondary Gortler Instability in Hypersonic Boundary Layers," *AIAA 2001-0273*, 2001.

[10] Lin, R., Malik, M. R., and Sengupta, R., "Computation of hypersonic boundary-layer response to external disturbances," *AIAA 99-0411*, 1999.

[11] Zhong, X., "Leading-edge receptivity to free-stream disturbance waves for hypersonic flow over a parabola," *J. Fluid Mech.*, Vol. 441, 2001, pp. 315–367.

[12] Hall, P., "Görtler vortices in growing boundary layers: the leading edge receptivity problem, linear growth and the nonlinear breakdown stage," *Mathematika*, Vol. 37, 1990, pp. 151–189.

[13] Danier, J. P., Hall, P., and Seddougui, S. O., "On the receptivity problem for Görtler vortices: vortex motion induced by wall roughness," *Phil. Trans. R. Soc. Lond. A*, Vol. 335, 1991, pp. 51–85.

[14] Whang, C. and Zhong, X., "Receptivity of Görtler vortices in hypersonic boundary layers," *AIAA 2002-0151*, 2002.

[15] Zhong, X., "High-order finite-difference schemes for numerical simulation of hypersonic boundary-layer transition," *J. Comput. Phys.*, Vol. 144, 1998, pp. 662–709.

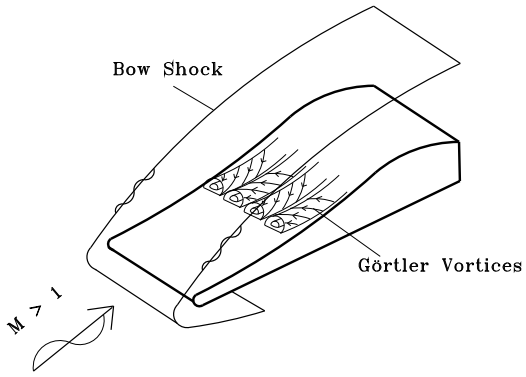

Figure 1: A schematic of computational domain of two-dimensional base flow and free stream receptivity of Görtler instability simulation.

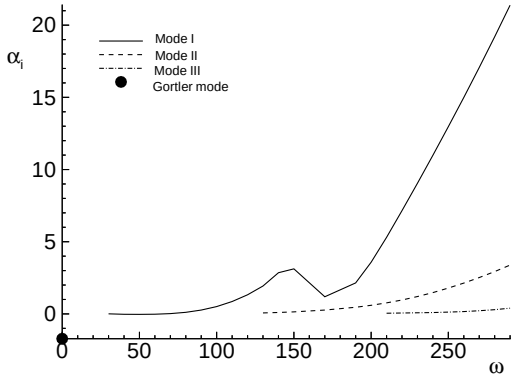

Figure 3: The growth rates (α_i) for various wave modes with respect to wave frequencies at the end of the computational domain.

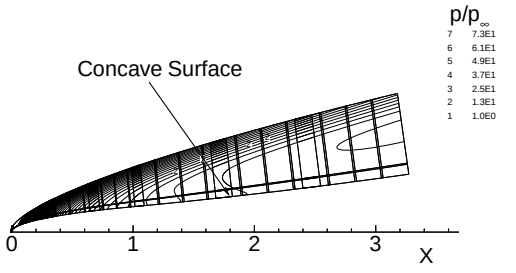

Figure 2: Pressure contours of 2-D numerical solution for high Reynolds number at $M_\infty = 15$.

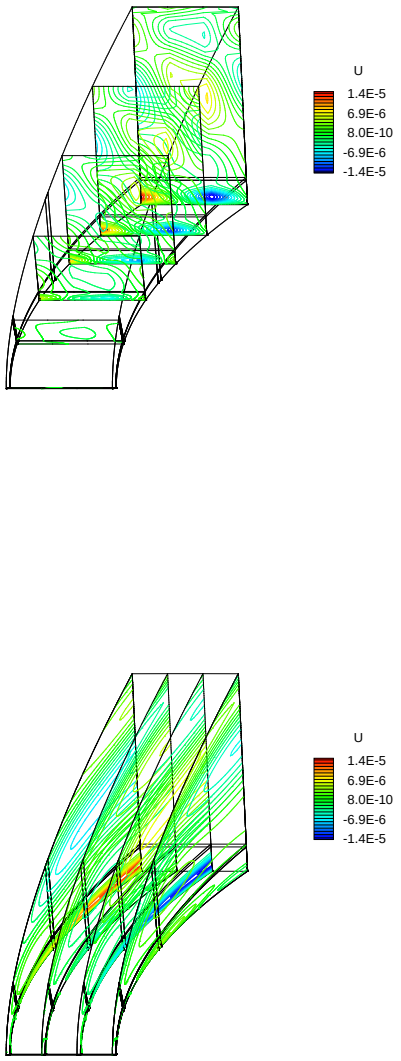

Figure 4: Streamwise velocity perturbation contours of the first computational zone. The figure shows growing disturbance inside boundary layer due to the early transient growth.

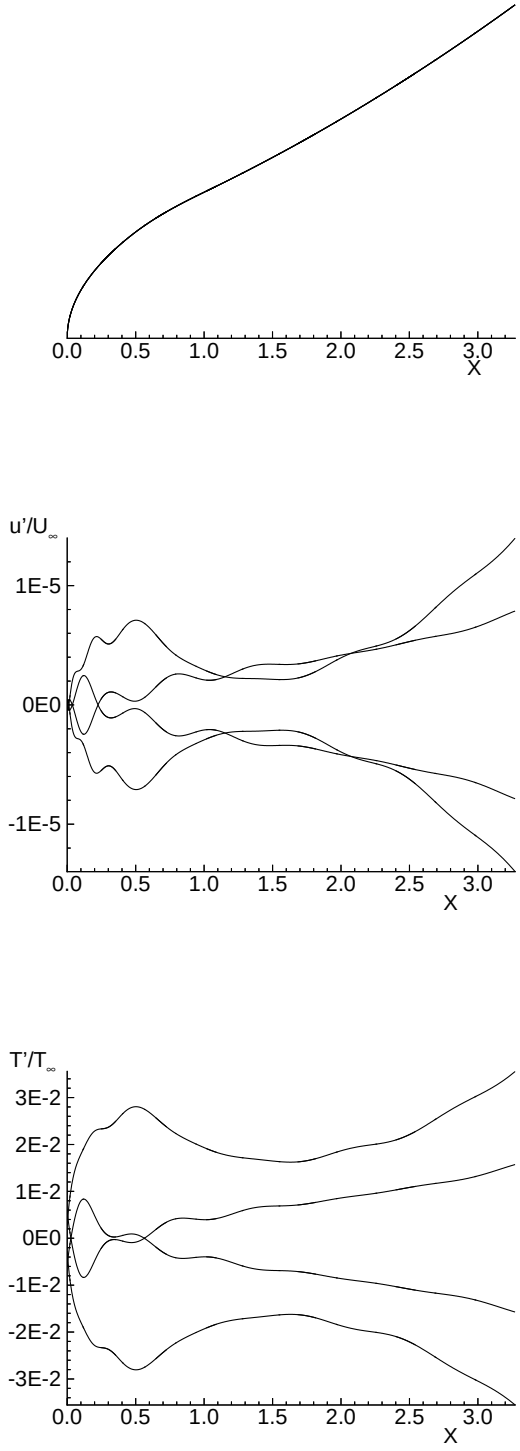

Figure 5: Surface shape and streamwise distributions of streamwise velocity and temperature perturbations induced by steady free stream vorticity waves.

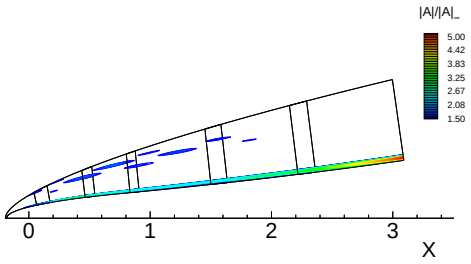

Figure 6: Streamwise distributions of maximum disturbance amplitude contours of velocity disturbances obtained by Fourier analysis at $\beta = 0.1$.

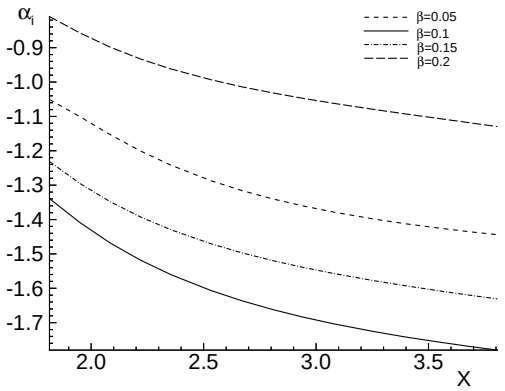

Figure 7: Streamwise distributions of unstable Görtler mode obtained from LST analysis

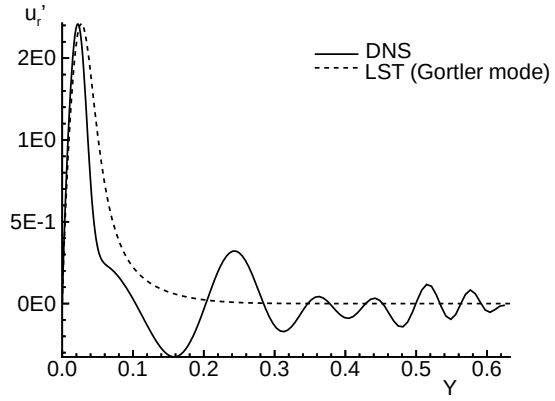

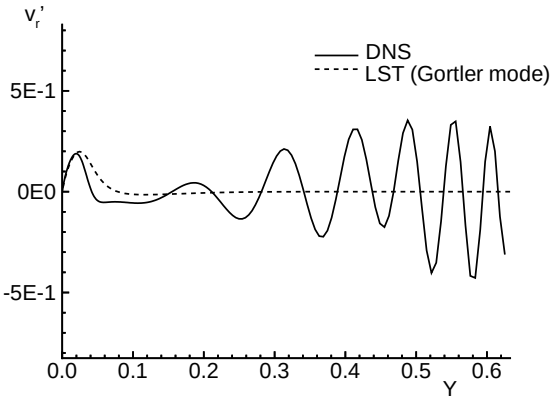

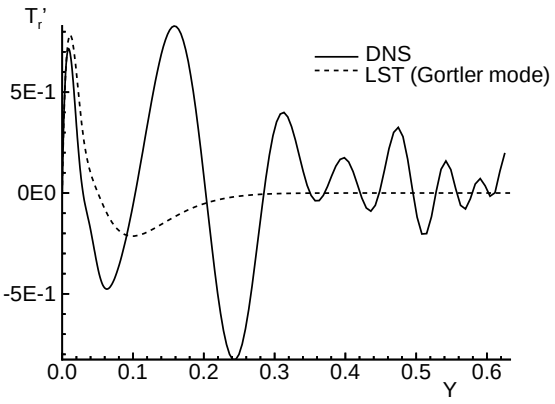

Figure 8: Comparison of DNS results of wall normal distributions of the disturbances with LST at $X = 3.0$.

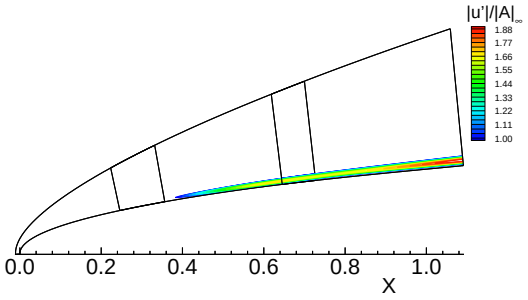

(a) $\beta = 0.05$

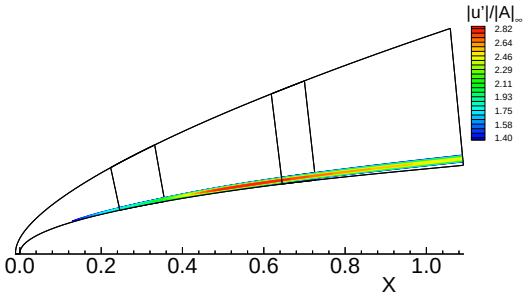

(b) $\beta = 0.10$

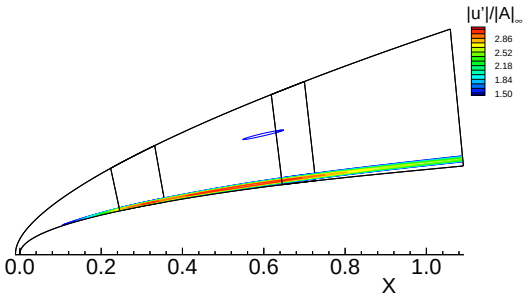

(c) $\beta = 0.15$

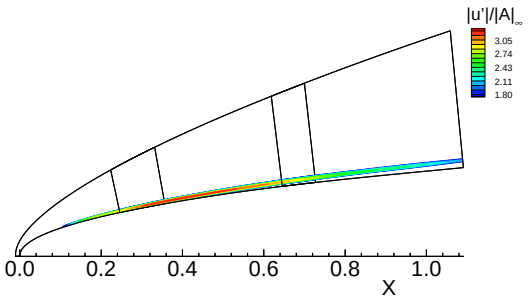

(d) $\beta = 0.20$

Figure 9: Amplitude contours of streamwise velocity perturbations in convex region including a blunt nose at four different spanwise wave number.

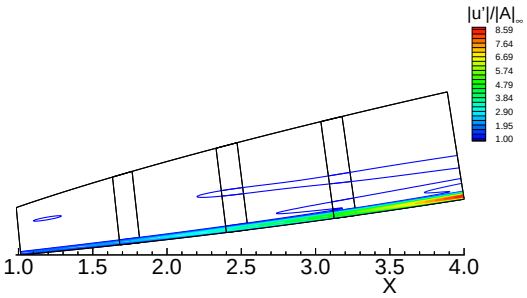

(a) $\beta = 0.05$

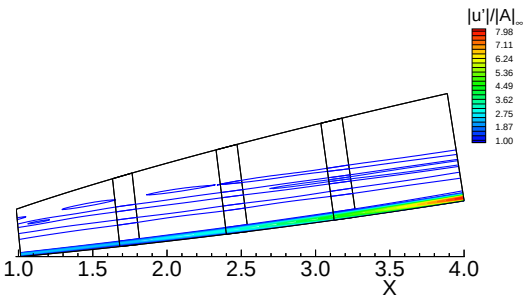

(b) $\beta = 0.10$

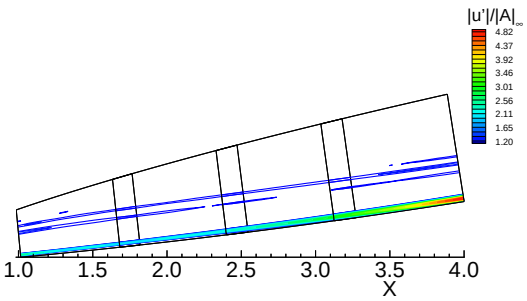

(c) $\beta = 0.15$

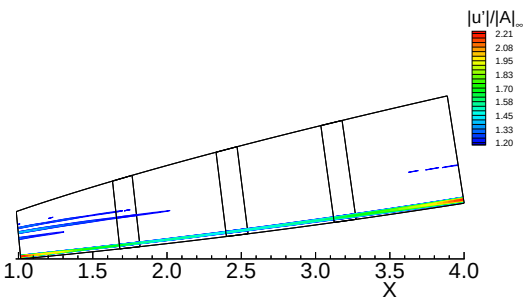

(d) $\beta = 0.20$

Figure 10: Amplitude contours of streamwise velocity perturbations in concave region at four different spanwise wave number.

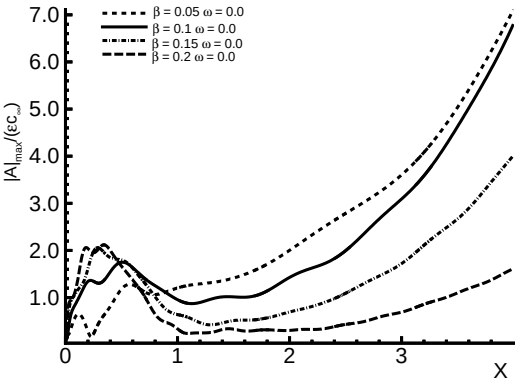

Figure 11: Streamwise distributions of maximum disturbance amplitudes inside boundary layers for four different spanwise wave numbers.

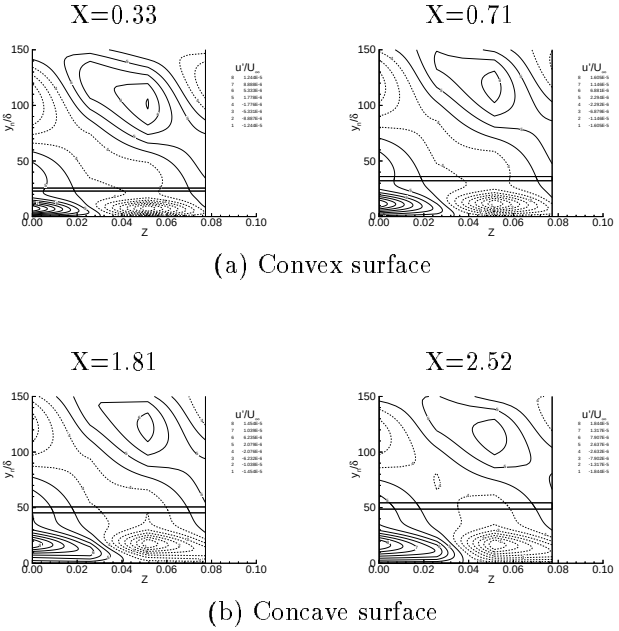

(a) Convex surface

(b) Concave surface

Figure 12: Streamwise velocity disturbance contours at four different streamwise locations. Basic structures in convex and conve region are the same.

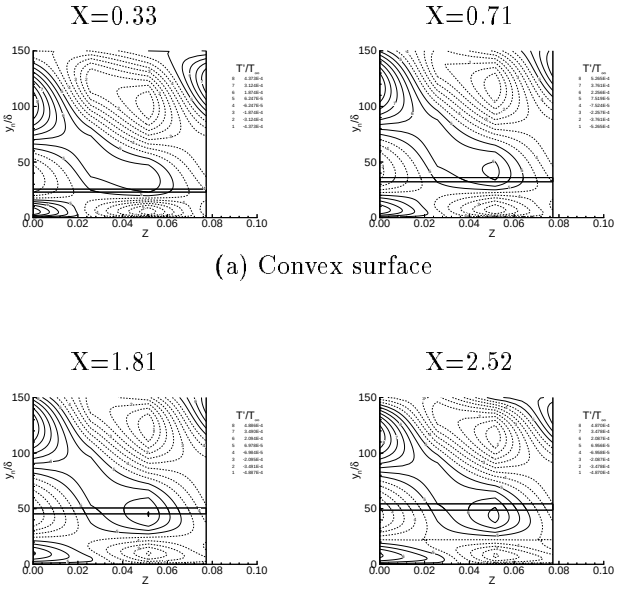

(a) Convex surface

(b) Concave surface

Figure 13: Temperature disturbance contours at four different streamwise locations.

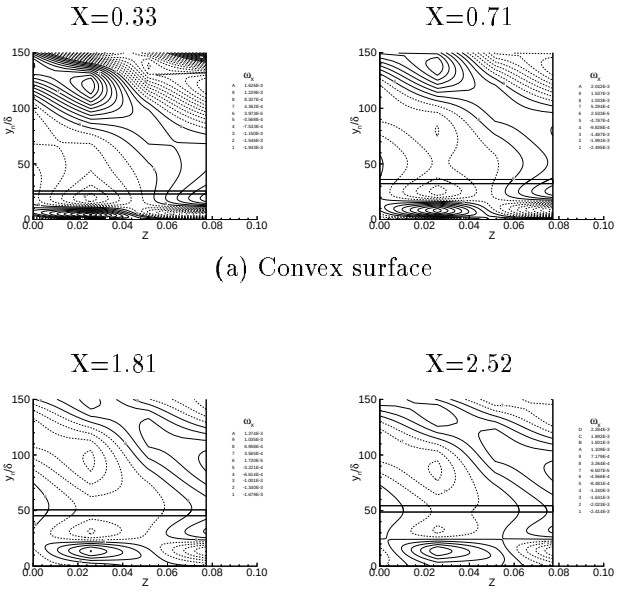

(a) Convex surface

(b) Concave surface

Figure 14: Streamwise vorticity contours at four different streamwise locations.

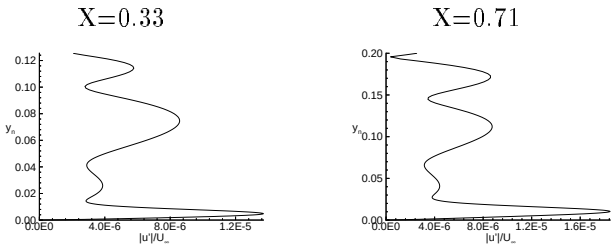

(a) Convex surface

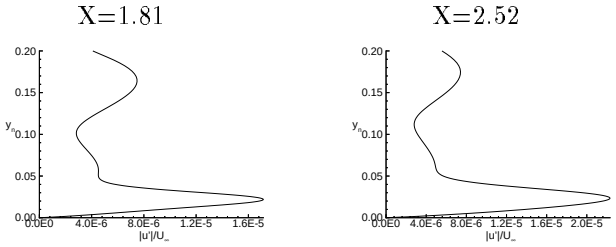

(b) Concave surface

Figure 15: Wall normal distributions of streamwise velocity disturbance amplitude at four different streamwise locations obtained from Fourier analysis.

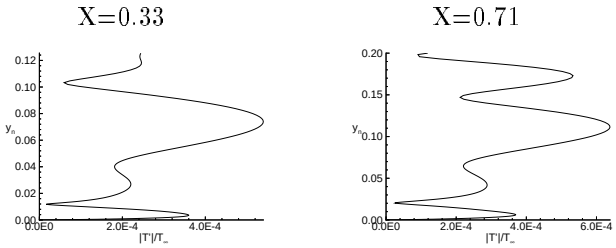

(a) Convex surface

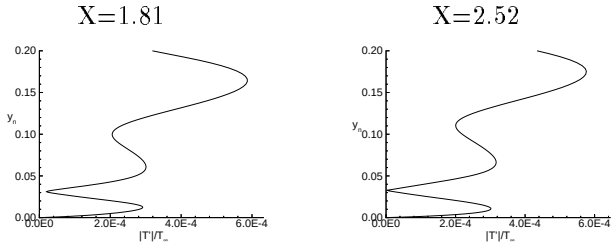

(b) Concave surface

Figure 16: Wall normal distributions of temperature disturbance amplitude at four different streamwise locations obtained from Fourier analysis.

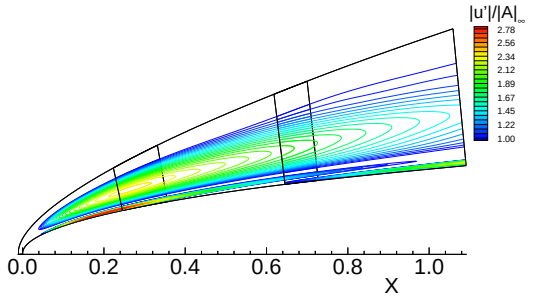

(a) $\theta = 0°$

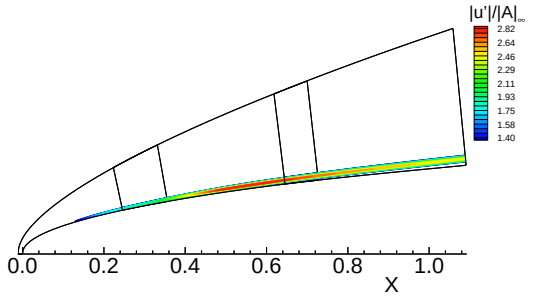

(b) $\theta = 30°$

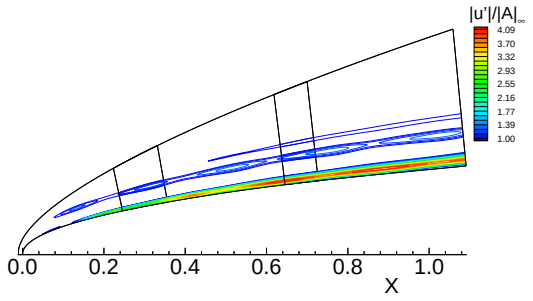

(c) $\theta = 60°$

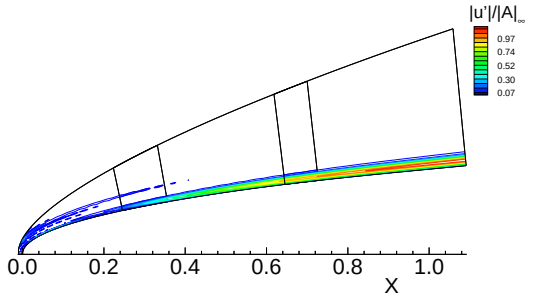

(d)$\theta = 85°$

Figure 17: Contours of streamwise velocity disturbance amplitude in convex region including a blunt nose at four different forcing wave angles.

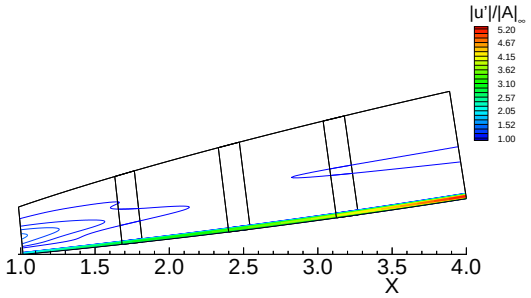

(a) $\theta = 0°$

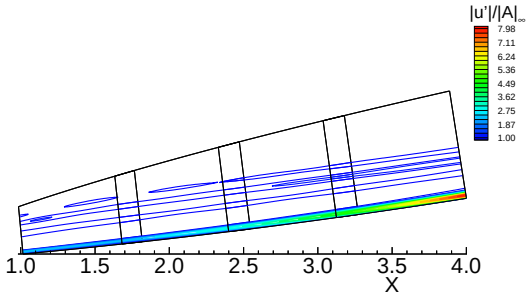

(b) $\theta = 30°$

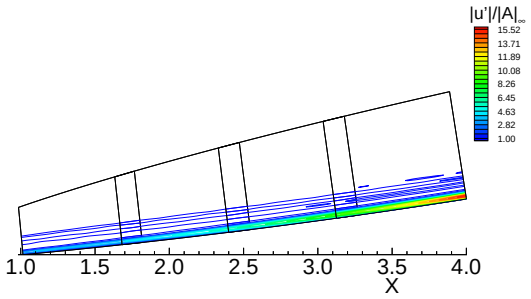

(c) $\theta = 60°$

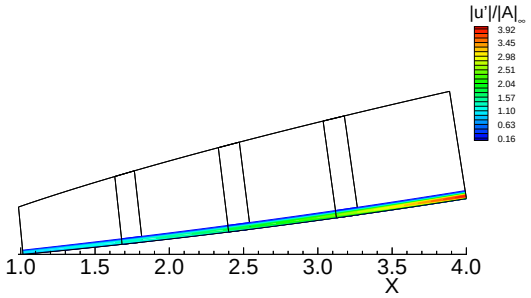

(d) $\theta = 85°$

Figure 18: Contours of streamwise velocity disturbance amplitude in concave region at four different forcing wave angles.

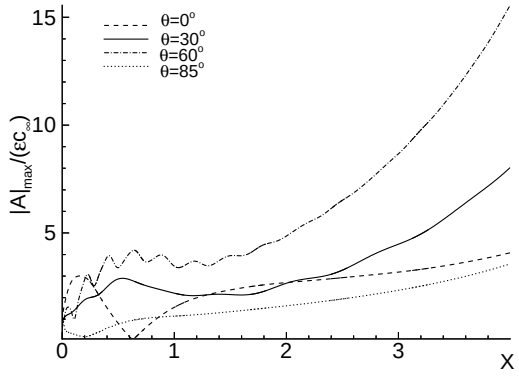

Figure 19: Streamwise distributions of maximum disturbance amplitudes inside boundary layers for four different wave angle, θ.

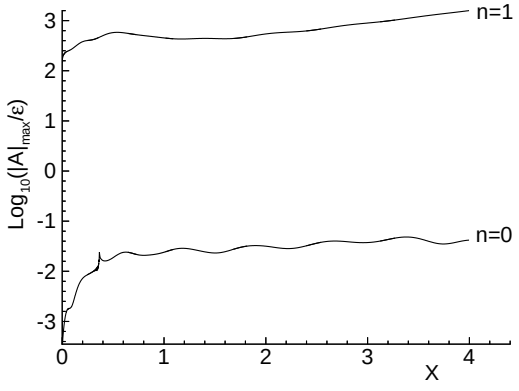

Figure 20: distributions of maximum disturbance amplitude for fundamental mode ($n = 1$) and mean flow correction mode ($n = 0$) at $\epsilon = 10^{-4}$

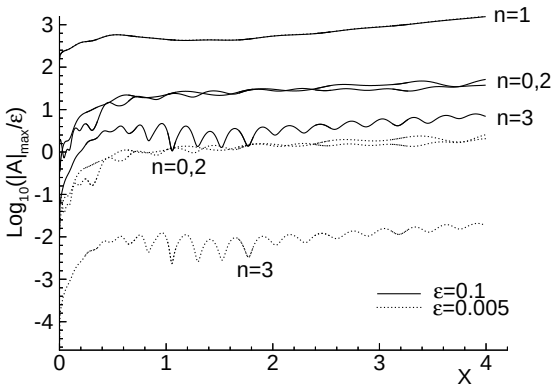

Figure 21: Distributions of maximum disturbance amplitudes inside boundary layers at two different ϵ.

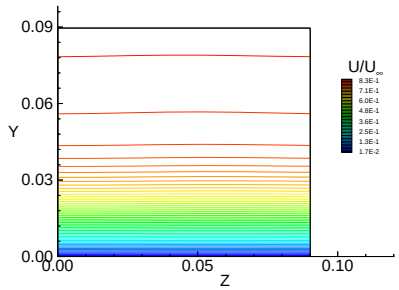

(a)$\epsilon = 5 \times 10^{-3}$

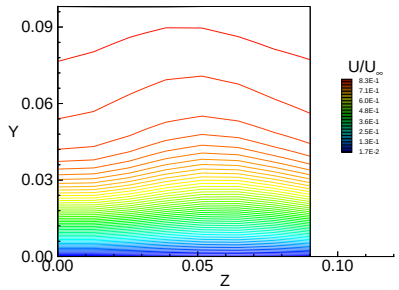

(b)$\epsilon = 10^{-1}$

Figure 22: Contours for the streamwise mean velocity (2-D base flow + Görlter mode) for two different forcing amplitudes at the end of computational domain.

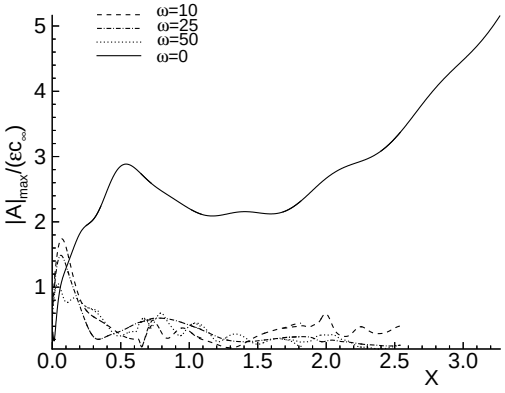

Figure 23: Comparison of the maximum disturbance amplitudes inside boundary layers of the traveling and standing free-stream vorticity waves.

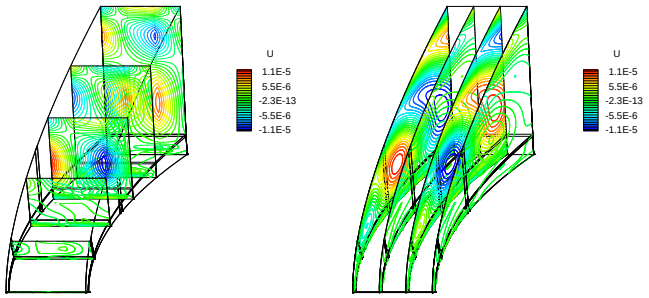

(a) $\omega = 25$

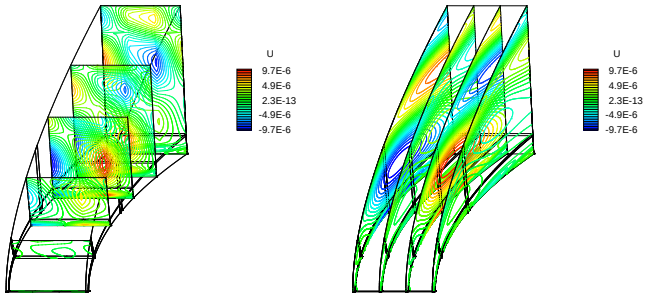

(b) $\omega = 10$

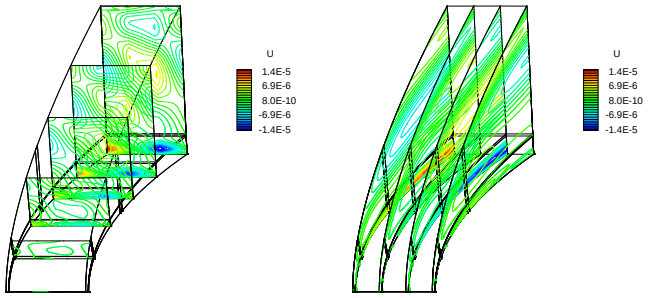

(c) $\omega = 0$

Figure 24: instantaneous cross sectional contours of streamwise velocity perturbations for the traveling and standing vorticity waves.

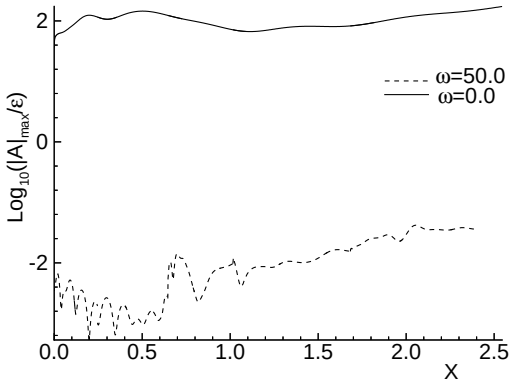

Figure 25: Comparison of the maximum disturbance amplitudes of mean flow correction mode of traveling vorticity waves with those for the standing waves.